Hindawi

Research Article

Effect of Fiber Content on Mechanical Properties and Microstructural Characteristics of Alkali Resistant Glass Fiber Reinforced Concrete

Chao Wu [iD],[1,2,3] **Xiongjun He** [iD],[1,2] **Xia Zhao** [iD],[4] **Li He** [iD],[5] **Yuan Song** [iD],[6]
and Xiuyan Zhang [iD][4]

[1]*School of Transportation and Logistics Engineering, Wuhan University of Technology, Wuhan 430063, China*
[2]*Hubei Province Highway Engineering Research Center, Wuhan 430063, China*
[3]*CERIS, Instituto Superior Técnico, Universidade de Lisboa, Lisboa 1049-001, Portugal*
[4]*Binzhou Polytechnic, Binzhou 256603, China*
[5]*School of Civil Engineering, Guizhou Institute of Technology, Guiyang 550003, China*
[6]*Hubei Communications Planning and Design Institute Co., Ltd, Wuhan 430051, China*

Correspondence should be addressed to Xia Zhao; yxzhaoxia@sina.com

Owing to its enhanced strength, ductility, and resistance to harsh environments, increasing research attention has been paid to alkali-resistant glass fiber reinforced concrete (ARGFRC). This paper presents experimental studies concerning the effects of fiber content on the mechanical properties and microstructural characteristics of ARGFRC. The amount of glass fiber was considered at levels of 0.0, 0.3, 0.5, 0.8, 1.0, 1.3, and 1.5% of the concrete volume. The compression, flexural, impact resistance, scanning electron microscopy, and energy dispersive spectroscopy tests were conducted. The flexural load-deflection curve, flexural strength, flexural toughness index, flexural fracture energy, postcracking stiffness, postpeak stiffness, and impact resistance energy absorption were obtained. Then the changing law affected by fiber content on these mechanical properties was further analyzed, and the corresponding equation was fitted. When fiber content was 1.5%, the flexural toughness index I_5, I_{10}, and I_{20} values were 4.0, 5.9, and 8.9, respectively, and increased by 3.0~7.9 times. Glass fiber incorporation could increase the ductility and delay the brittle failure when the fiber content reached 0.8%. The largest postcracking stiffness was calculated at 36.174 kN/mm with a fiber content of 0.8%. The higher the fiber content, the larger the postpeak stiffness of the tested beams. Impact resistance test results demonstrated that the optimum fiber content was 1.3%. As the fiber content increased, the effect of the concrete grout on the fiber packaging decreased, according to the scanning electron microscopy analysis. The energy dispersive spectroscopy observation proved that adding a certain fiber content did not affect the concrete hydration reaction.

1. Introduction

The development of modern engineering constructions has generated a high demand for new types of concrete needed to have improved properties such as strength, fracture, durability, and sustainability. There has been a steady increase over the last decades in the use of fiber-reinforced concrete (FRC) in the engineering field. FRC comprises hydraulic cement, aggregates, and discrete reinforcing fibers [1]. FRC has received worldwide attention due to its advantageous material properties, including high initial crack strength, tensile and compressive strength, toughness, outstanding impact resistance, and excellent energy absorption capacity [2–5]. Afroughsabet et al. provided a comprehensive review of the mechanism of crack formation and propagation and the mechanical properties of high-performance FRC [2]. Yin et al. [3] presented the preparation techniques and the properties of macroplastic fibers, and the effects of macroplastic fibers on the fresh and hardened concrete performances were discussed as well. Yoo

and Banthia studied the impact resistance of FRC; the impact test methods were addressed, and the comprehensive impact resistance of FRCs subjected to various loading conditions with different fibers was investigated [4]. Ahmad and Zhou discussed the mechanical performances of concrete reinforced with natural or synthetic fibers. The recommended fiber content addition by weight was up to 1.0% of the maximum mechanical properties of FRC, while further addition of fibers decreased the mechanical performances due to the lack of workability [5]. FRC's mechanical properties [6–10], such as tensile strength, compressive strength, flexural strength, fracture toughness [6, 11–13], impact resistance [12, 13], and microstructural characteristics [14, 15], were investigated. Söylev and Özturan concentrated on the mechanical properties of a low-volume fraction (0.5% steel fibers + 0.1% polypropylene, 0.1% glass fiber) FRC [6]. The effect of moist curing was more favorable for compressive and splitting tensile strengths of FRCs, while this effect was more emphasized in compressive compared to splitting strength. Dehghan et al. [7] demonstrated that the compressive strength and drying shrinkage were not promoted by recycled glass fiber reinforced polymer and virgin E-glass fiber additions at a substitution level of 5 wt% of the coarse aggregate, while the splitting tensile strengths were improved in most cases. Gopalaratnam and Gettu [8] pointed out the suggestions to improve the toughness characterization while adopting the four-point bending test on unnotched FRC beams. Furthermore, the equivalent post-cracking strength approach provided an elegant way to consider energy absorption in design. Bakhshi et al. [9] evaluated the effects of early age and fiber type on the FRC toughness parameters, including the back-calculated tensile stress-strain response along with simulated and tested flexural load-deflection curves. Gopalaratnam et al. concluded that the initial crack deflection of FRC can vary by as much as an order of magnitude relying on the methodology adopted to measure deflections. The relative magnitudes of the extraneous deformation rely upon the test setup and load-carrying capacity of the FRC beam [11]. Enfedaque et al. depicted more fibers being pulled out of the matrix instead of broken in aged glass FRC (GFRC) scanning electronic microscope (SEM) samples, owing to the addition of metakaolin [14]. Yuan and Jia [15] studied the effects of glass fiber (GF) and polypropylene fiber (PPF) on the microstructural characteristics of FRC as a function of fiber content and water/binder ratio. The results demonstrated that the water/binder ratio affected the optimal fiber content based on the preliminary analysis of the SEM observation. The improvement effect of GF on water absorption was superior to that of PPF. The influencing factors of the FRC properties have been explored, such as fiber types [12, 15–17], fiber content [16], and fiber dispersion. Vafaei et al. investigated the static and dynamic fracture behavior of high-strength fiber-reinforced seawater sea-sand (SWSS) concrete by conducting fracture toughness and drop weight impact tests. Polyvinyl alcohol and polypropylene fibers (PPFs) with different fiber contents (0.1%–0.5%) were used for reinforcement. Incorporating PPF improved both the static and dynamic fracture

performances of SWSS FRC [12]. Ghadban et al. studied the effect of fiber type (steel fiber and synthetic fiber) and content on the flexural performance of FRC for highway bridges. Steel FRC (SFRC) presented superior flexural performances compared to synthetic FRC. Notwithstanding, SFRC was susceptible to corrosion and twice as expensive as synthetic fibers [16]. Yang et al. [17] demonstrated that 1.0% steel fiber and 1.0% glass fiber presented the best improvement effects on the compressive strength and impermeability of recycled concrete. Madhkhan and Katirai [10] used AR glass fibers (ARGFs) with three different types of pozzolanic materials in GFRC and found that the toughness index and modulus of rupture decreased over time due to aging. Kimm et al. proposed different surface treatments to protect fiber-reinforced polymer fragments in concrete and improve adhesion. A sanded surface of glass fiber polymers increased the average maximum shear stress by 16%, according to the pull-out tests [18]. Ali et al. [19] manufactured FRC by incorporating 0.5 and 1.0% volume fractions of GF, hooked steel fiber (HSF), and polypropylene fiber (PPF). FRC pavement with 0.5% HSF, 0.5% GF, 1% GF, 0.5% PPF, and 1% PPF indicated 4%, 18%, 17%, 13%, and 18% lesser carbon emissions of pavement compared to plain concrete, respectively. Lin et al. [20] studied the coupling effects of expansive agents (EAs) and GFs on the splitting strength and fracture properties of SWSS concrete. The combined usage of EAs and GFs maximally increased the splitting strength, flexural strength, fracture energy, and initial and unstable fracture toughness indexes by 65%, 75%, 155%, 101%, and 82%, respectively. Saidani et al. [21] demonstrated that steel, macro-fiber, and micro-polypropylene change the failure types to ductile failures, thus overcoming concrete's brittleness issue and improving its split tensile strength. Çelik and Bingöl [22] investigated the impact strength and fracture properties of self-compacting concrete reinforced with basalt fiber (BF), GF, and PPF, and it was suggested that the addition of BF, GF, and PPF all increased the flexural strength, impact resistance, and fracture energy. Surveys conducted by Aghdasi et al. [23] suggested that steel FRC (SFRC) could be developed for large-scale structural applications by changing mixture components and fiber volume fractions. Steel fibers are one of the most attractive preferences because they are widely available and affordable. Conversely, SFRC poses unavoidable disadvantages, such as increased self-weight, decreased workability, fiber balling at high contents, and susceptibility to corrosion. Simultaneously, synthetic fibers also have a low modulus of elasticity, a low melting point, and weak interfacial bonding with cementitious matrixes [24]. Therefore, GF is a popular substitute to reimburse for this vulnerability. Adopting GFRC could significantly improve the design of concrete structures, offer endless design possibilities in architecture, and be more cost-effective than other alternatives. The distinguished interaction of two basic materials, concrete matrix and GF, safeguards the good mechanical properties of GFRC [25].

Despite the significance and concerns about the behavior of GFRC, studies on this topic are still quite limited, namely about the effects of fiber volume content on the mechanical

and microscopy properties of GFRC. The most relevant issues of earlier investigations in this specific research field are illustrated, along with the aspects that still require extra research efforts and motivate the present investigation. Arslan [26] analyzed the effects of chopped glass fibers' incorporation on fracture energy and mechanical properties of normal-strength concrete using crack mouth opening displacement (CMOD) measurement. Three-point bending tests were also performed on notched beams produced using GFRC with 0.5, 1, 2, and 3 kg/m^3 fiber contents to determine the value of fracture energy. GF has been used in concrete for controlling early-age microcracks (EAMC) in bridge decks. The experiments illuminated a decrease in compressive strength and an increase in splitting tensile and flexural strengths of GFRC compared to plain concrete (PC) [27]. Yuan and Jia [15] reported that the content of GF affected the slump and the flexural properties; when the slump decreased, average residual strength, equivalent flexural strength ratio, toughness, and modulus of rupture increased with increasing fiber content [16]. No flexural strength increased with a high fiber content of GFRC, while more than 0.50% fiber content was added in high-strength GFRC. Furthermore, fracture energy increased significantly when more than 0.25% fiber content was used for GFRC [28]. Incorporating chopped GFs with fiber volume fractions between 0% and 2% into ceramic concrete leads to significant increases in flexural strength and direct shear strength, regardless of the matrix type or fiber length [29]. Static tests in compression, tension, and bending were performed. Dynamic tests using a modified Hopkinson bar were conducted to figure out how GF affected energy absorption and tensile strength of the fiber-reinforced mortar at a high strain rate. The experimental results demonstrated that adding GF significantly increased energy absorption at a high strain rate [30]. The effects of alkali-resistant GF (ARGF) volume fractions of 0.125–0.75% on the flexural strength and ductility, restrained shrinkage cracking of lightweight GFRC were investigated, and fiber volume fractions of 0.25–0.5% were sufficient for control of restrained shrinkage cracks and enhancement of the flexural toughness [31]. Incorporating low-volume fractions of two types of ARGF can control the cracking that develops due to early age shrinkage on both standard concrete and SCC in two diverse ways, namely by reducing the total cracked area and the maximum length of the cracks. The microscopic study of cracked surfaces verifies the encouraging effect of the presence of dispersed ARGFs on cracking control [32]. The effects of ARGF with fiber content varying from 0.5 to 4.5% by weight of cement on different strengths (compressive, flexural, split tensile, and bond) of M20 grade concrete were considered [33]. Single fiber model composites of ARGFs and a cementitious matrix were adopted to interrogate the pull-out behavior under quasistatic and high-speed loading. Results testified that the interface between ARGFs and the concrete matrix behaved normally, without obvious slip-hardening or slip-weakening effects, in both quasi-static and high-rate pull-out tests [34]. GFRC with and without polymer was used as the benchmark material to evaluate concrete self-healing enhanced by crystalline admixture. Results showed a difference in the self-

healing start between GRC and PGRC samples [25]. Scanning electron microscopy (SEM) photographs indicated that incorporating metakaolin enabled more fibers to be pulled out of the matrix rather than broken in aged GFRC samples [14]. Thus far, studies have highlighted factors associated with recycled GF used in FRC [7, 35–37]. Zhao et al. investigated the constitutive model of ARGFRC with four different fiber volume contents (0.0%, 0.5%, 1.0%, and 1.5%). Results indicated the optimal load-bearing capacity of GFRP (glass fiber reinforced polymer) reinforced GFRC beam was at 1.0% fiber content [38]. Le et al. proposed a constitutive model of FRC by incorporating microcracking and fiber-bridging mechanisms [39]. Yang et al. studied the properties of ARGF reinforced coral aggregate concrete [40]. Wang et al. experimentally investigated the properties of graded GFRC based on the construction of tunnel engineering applications to avoid partition wall cracking and lining seepage [41].

The studies reviewed above confirmed the susceptibility of mechanical, durability, and microstructural properties for GFRC at different fiber contents. Nevertheless, the information they provided about the behavior of different fiber contents was not always and completely consistent. The following gaps are being highlighted: (i) Arslan's experiments [26] clarified that the flexural strength of GFRC increased with fiber content, whereas there was a slight downturn for a high volume of fiber content. Meanwhile, in other studies [16, 29], the flexural properties increased with high fiber content, and no flexural strength increase was observed by Kizilkanat et al. [28] when fiber content was more than 0.5%. Much uncertainty still exists about the relationship between fiber content and the mechanical properties of GFRC. The optimal fiber content of ARGFRC is still unclear considering various aspects of its mechanical properties and application scenario. (ii) The mechanism by which fiber content affects the SEM and energy dispersive spectroscopy (EDS) has not been adequately established.

Consequently, this study aimed to fulfill the research gaps mentioned above and better understand the effects of fiber content on the mechanical and microstructure properties of alkali resistant glass fiber reinforced concrete (ARGFRC). Homoplastically, a systematic investigation of the compressive strength, flexural toughness, and impact resistance of ARGFRC was experimentally conducted. SEM and EDS microstructural analyses of ARGFRC were performed as well, which will provide references to the research and practical engineering applications of ARGFRC in civil engineering infrastructures.

2. Materials and Methods

2.1. Materials and Mix Proportions. The cement used in the experiment was ordinary Portland cement with a strength grade of 42.5R, and the cement stability met the specified requirements from GB 175-2007 [42]. The apparent sand density and bulk density were 2710 kg/m^3 and 1600 kg/m^3, respectively. The sand porosity was 45.00%, and the stone powder content was 5.10%. For concrete compressive

strength grades ranging from C30 to C55, the requirement for stone powder content should be less than 7.00% regarding JGJ 52-2006 [43]. According to JGJ52-2006 [43] and the sand sieving properties provided in Figure 1, the sand fineness modulus was 2.9, and the sand particle grading belonged to region II. Crushed stone per JGJ 52-2006 [43] has an apparent density, bulk density, porosity bulk density, crushing index, mud content, and needle-like particle content of 2700 kg/m^3, 1420 kg/m^3, 47.00%, 9.90%, 0.50%, and 4.00%, respectively. The FMY-1 water-reducing agent adopted was recommended by GB 8076-2008 [44]. Local tap water based on JGJ 63-2006 [45] was used.

The GF adopted in the experiment was alkali-resistant GF (ARGF), a high-performance short-cutting original wire was used to increase the mechanical performance of concrete and is applied to concrete and cement mortar. Compared to other types (plastic shrinkage control, sprayed yarn, repair mortar, and premixed mortar) of ARGF, this kind of ARGF was especially used in bridge concrete structures aiming at controlling and preventing cracking in concrete. By adding ARGF to concrete, there are advantages such as effectively improved flexural and impact properties, good processability with the surface almost out of sight; availability for high volume incorporation without affecting the workability; no trace on the surface; homogeneous mixing without requiring additional water; safe and straightforward operation. The surface treatment methods of glass fiber are generally divided into heat treatment methods and chemical treatment methods. Chemical treatment methods of glass fiber generally include acid alkali etching treatment and silane coupling agent coating treatment. The essence of silane coupling agent surface treatment is to graft the silane coupling agent onto the surface of glass fiber through chemical bonding. The treatment mechanism is that the silanol generated after the hydrolysis of organ silane reacts with the hydroxyl group on the surface of glass fiber to form a stable Si-O-Si bond. Diluted silane solution (pH = 3~4) was prepared by using pure silane with 80% ethanol, 10% acetic acid, and 10% aqueous solution. The silane surface treatment adopted a weight concentration of the diluted silane versus ARGF of 0.2 : 100 in an ultra-mixing machine at 100 rpm for five minutes and then a drying process in an oven at 140°C for 4 h [46]. The ARGF properties presented in Table 1 were obtained from the manufacturer, Taishan Fiberglass Inc. This type of ARGF was specially applied in the negative moment zone of bridge concrete slabs to prevent concrete cracks. The original fiber wire diameter was 14–19 μm according to ISO 1888:2006 [47], the loss on ignition was 0.80–2.0%, in line with ISO 1887:1995 [48], and the moisture content was less than 0.50% per ISO 3344:1997 [49]. The tensile strength of ARGF was 1700 MPa as per ASTM D 2343-17 [50]. The specific gravity and softening temperature of ARGF were 2.68 g/cm^3 and 860°C, respectively. The fiber length was 36 mm, and the modulus of elasticity was 72 GPa.

Specimens were cast according to the code for the design of concrete structures, with 28 days to reach the target strength of 40 MPa. In the whole concrete mixture design
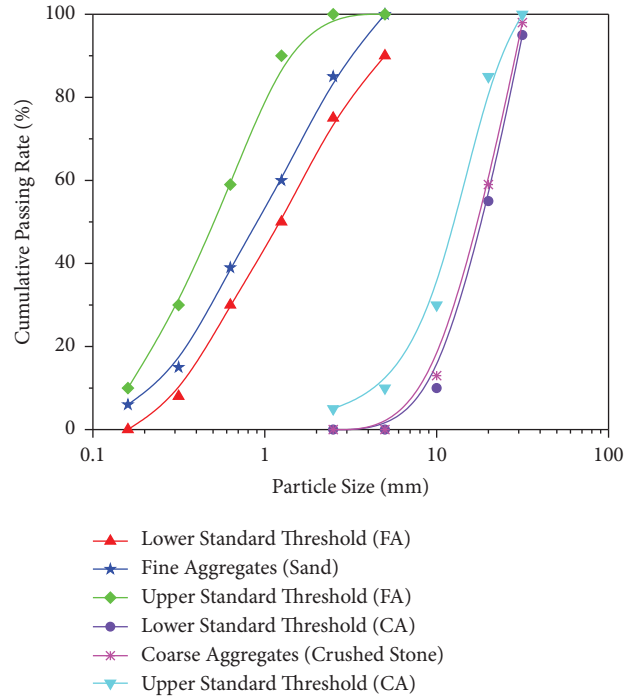

Figure 1: Particle size distribution of the aggregates.

Table 1: ARGF properties.

Property	Value
Fiber length (mm)	36
Fiber length to diameter ratio	58
Original wire diameter (μm)	14–19
Loss on ignition (%)	0.80–2.00
Moisture content (%)	≤0.50
Specific gravity (g/cm^3)	2.68
Modulus of elasticity (GPa)	72
Tensile strength (MPa)	1700
Softening temperature (°C)	860
Color	White to off-white

process, the mixture design of cement, fine natural aggregate, coarse natural aggregate, and water was 1 : 1.40 : 2.09 : 0.40 [38, 51]. The amount of water-reducing agent was 3.0 kg per cubic meter of concrete. The volume incorporation of ARGF content was 0.0%, 0.3%, 0.5%, 0.8%, 1.0%, 1.3%, and 1.5%, respectively. The specific mixture proportion design of ARGFRC was displayed in Table 2.

2.2. Specimen Preparation and Curing. During the ARGFRC specimen preparation process, the following two steps were included in the concrete mixing procedure: (i) Adding cement, fine natural aggregate (river sand), coarse natural aggregate (stone), water, and a water-reducing agent to the concrete mixer to mix for two minutes. (ii) Adding all the ARGF gradually to the concrete mixer and mixing the fresh ARGFRC for at least one minute. The ARGFRC mixing process should guarantee that ARGF is evenly and randomly distributed in the concrete specimens to prevent fiber agglomeration [52]. Due to the slump being 45 mm

TABLE 2: ARGFRC mixture proportion design.

Component	FC0	FC0.3	FC0.5	FC0.8	FC1.0	FC1.3	FC1.5
Cement (kg/m^3)	500	500	500	500	500	500	500
Stone (kg/m^3)	1045	1045	1045	1045	1045	1045	1045
River sand (kg/m^3)	700	700	700	700	700	700	700
Water (kg/m^3)	200	200	200	200	200	200	200
Water-reducing agent (kg/m^3)	3.0	3.0	3.0	3.0	3.0	3.0	3.0
Fiber volume content (m^3)	0.0%	0.3%	0.5%	0.8%	1.0%	1.3%	1.5%

Note. FC-0.5 indicates 0.5% fiber content (by volume) of ARGFRC.

(less than 50 mm), the electronic vibration table was used for tamping and vibrating the concrete mixture in the steel specimen mold [52]. The specimen's surface was covered with plastic film immediately after forming. The specimens were kept static for 1–2 days in a room with a temperature of $20 \pm 5°$C and a relative humidity greater than 50%, they were named according to the specimen specification. After demolding, the specimens were put into a standard curing room for curing and placed on the support with an interval of 10–20 mm. The temperature of the standard curing room was $20 \pm 2°$C, and the relative humidity was above 95%. The surface of the standard curing specimens was kept moist, but rinsing the specimens with water was not allowed. The standard curing periods for compressive specimens were 7–28 days, while the flexural and impact specimens' curing duration was 28 days [52]. A total number of 42 ARGFRC cubes (dimension: 100 mm × 100 mm × 100 mm) were cast to obtain the cubic compressive strength for seven fiber contents and two standard curing periods (7 days and 28 days). Each fiber content was prepared with three specimens, and two trial runs were done to achieve the compressive strength of the two curing periods [52, 53]. Twenty-one ARGFRC beams (dimension: 100 mm × 100 mm × 350 mm) with a standard curing period of 28 days were prepared to conduct the flexural test per the standard recommended by the American Society for Testing and Materials Standard (ASTM) C1609/C1609M-19a [41], each fiber content cast with three specimens. As stated in CECS 13-2009 [52], a total of 42 ARGFRC columns (150 mm diameter and 63 mm height) were cast to investigate the impact properties, with six specimens for each fiber content after 28 days of standard curing.

2.3. Test Procedures

2.3.1. Compression Test.
A full-automatic pressure testing machine was adopted to conduct the compressive strength test regarding GB/T 50081-2019 [53], as demonstrated in Figure 2. During the test, it shall be loaded continuously and evenly, and the loading speed should be 0.5 MPa/s~0.8 MPa/ s. The cubic compressive strength of ARGFRC can be calculated as shown in equation (1) [53].

$$f_{cc} = \frac{F}{A},\tag{1}$$

where f_{cc} = the cubic compressive strength of concrete (MPa); F = the damage load of the specimen; A = the cross-section of specimen.

FIGURE 2: ARGFRC compression test.

2.3.2. Flexural Test.
A four-point bending loading test with a spreader beam placed on the third point was applied to the flexural test beams to study the flexural strength and flexural toughness. As the ARGFRC schematic flexural test shown in Figure 3, the distance from the spreader beam's left loading point to the left support of the test beam was 100 mm, and the support was 25 mm from the test beam end on each side. The adopted test equipment was a model WEW-1000B hydraulic universal testing machine (manufactured by Changchun New Testing Machine Co. Ltd, China). The range of its display value was 0–1000 kN, the resolution was 0.1 kN, and the loading rate was controlled at 0.05 mm/min. The flexural strength of FRC was calculated according to the following equations [52–54]:

$$f_f = \frac{Fl}{bh^2},\tag{2}$$

$$f_{cr} = \frac{F_{cr}l}{bh^2}.\tag{3}$$

Where f_f = flexural strength of concrete; F = damage load of specimens; l = support span; h = cross-section height of the specimen; b = cross-section width of the specimen; f_{cr} = initial crack flexural strength of concrete; and F_{cr} = initial crack load.

The calculation methods for the flexural toughness index were successively put forward by the American Concrete Institute (ACI) 544.9R-17 [55], Japan Concrete Institute (JCI) SF4 [56], and ASTM C1018 [57]. The flexural toughness index I_5, I_{10}, and I_{20} was proposed according to ASTM C1018 [57]. The flexural toughness calculation schematic diagram was illustrated in Figure 4. The O was the original point, following 1.0, 3.0, 5.5, and 10.5 in multiples of initial crack deflection δ_{cr}. On the horizontal axis, points B,

(a)   (b)
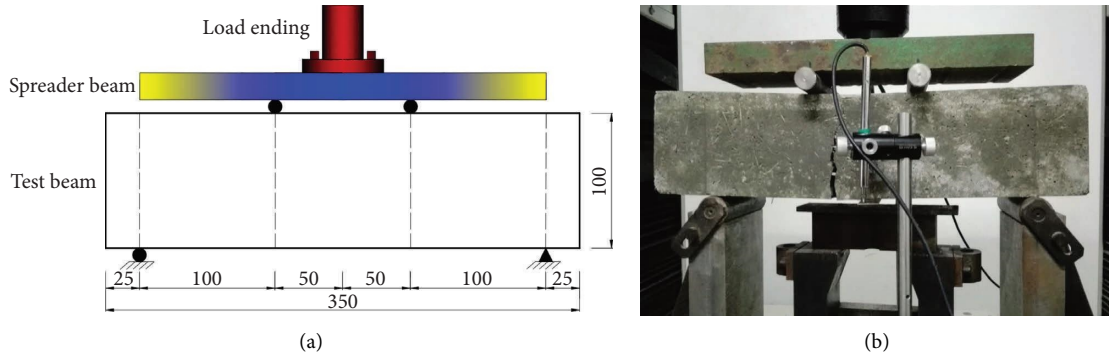
FIGURE 3: ARGFRC flexural test: (a) schematic diagram (unit: mm); (b) four-point bending test.

D, F, and H were determined, with a planimeter to measure the area of OAB, OACD, OAEF, and OAGH, which could be named as Ω_δ, $\Omega_{3\delta}$, $\Omega_{5.5\delta}$, and $\Omega_{10.5\delta}$, respectively. The flexural toughness index of each specimen was calculated according to the following Equations [10, 52, 57]:

$$I_5 = \frac{\Omega_{3\delta}}{\Omega_\delta}, \tag{4}$$

$$I_{10} = \frac{\Omega_{5.5\delta}}{\Omega_\delta}, \tag{5}$$

$$I_{20} = \frac{\Omega_{10.5\delta}}{\Omega_\delta}. \tag{6}$$

Aiming to accurately evaluate and compare the energy absorption, ductility, and strength sustainability of the test beams, two alternative stiffness approaches were utilized: post-cracking stiffness, which considered the beam stiffness after initial cracking until the peak load was reached, therefore evaluating the nonlinear postcracking behavior. And postpeak stiffness is considered the beam stiffness after the peak load until the maximum midspan deflection is reached (at beam failure), therefore evaluating the nonlinear postpeak behavior. In this light, postcracking stiffness, D_{PC} is calculated using the following equation [58, 59]:

$$D_{PC} = \frac{F_{\text{peak}} - F_{cr}}{\delta_{\text{peak}} - \delta_{cr}}, \tag{7}$$

where F_{peak} = the measured maximum force; F_{cr} = the load at initial cracking; δ_{peak} = the mid-span deflection at peak force (F_{peak}); and δ_{cr} = the mid-span deflection at initial cracking.

Similarly, post-peak stiffness, D_{PP}, may be calculated using the following Equation [58, 59]:

$$D_{PP} = \frac{\delta_{ult} - \delta_{\text{peak}}}{F_{\text{peak}} - F_{d,ult}}, \tag{8}$$

where δ_{ult} = the maximum midspan deflection as determined from the load-displacement relationship; and $F_{d,ult}$ = the load corresponding to the maximum measured midspan deflection that relates to a beam's ability to recover and sustain a high-strength, postpeak state.
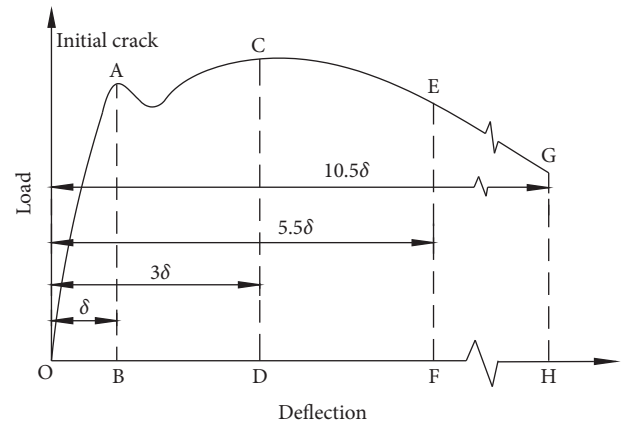

FIGURE 4: Computing models of flexural toughness index of FRC.

2.3.3. Impact Test. Self-made test instrumentation was implemented on the drop hammer impact resistance test based on the recommendations from ACI 544.9R-17 [52, 55]. The test principle was to accumulate a certain amount of energy until it was damaged, and then the absorbed kinetic energy was calculated. The impact resistance test setup consisted of an impact rack, an impact ball, and an impact hammer, as shown in the diagram in Figure 5(a). The distance between the two baffles on the bottom plate was 160 mm, and the distance from the impact rack to the impact ball surface was 500 mm. The diameter of the impact ball was 63 mm, and the mass of the impact hammer was 4.5 kg. In the top view of the impact resistance test, as demonstrated in Figure 5(b), the impact hammer moved in free fall, and the impact steel ball was placed on the top surface of the impact resistance specimen. Each impact was a cycle. When the initial crack appeared on the surface of the specimen, the number of initial impacts was recorded as N_1. Continuing to repeat the impact cycle until the specimen contacted any three of the four baffles of the impact frame, the number of failure impacts was recorded as N_2. According to the following equations, the initial crack resistance energy dissipation and failure resistance impact energy of ARGFRC were calculated [55]:
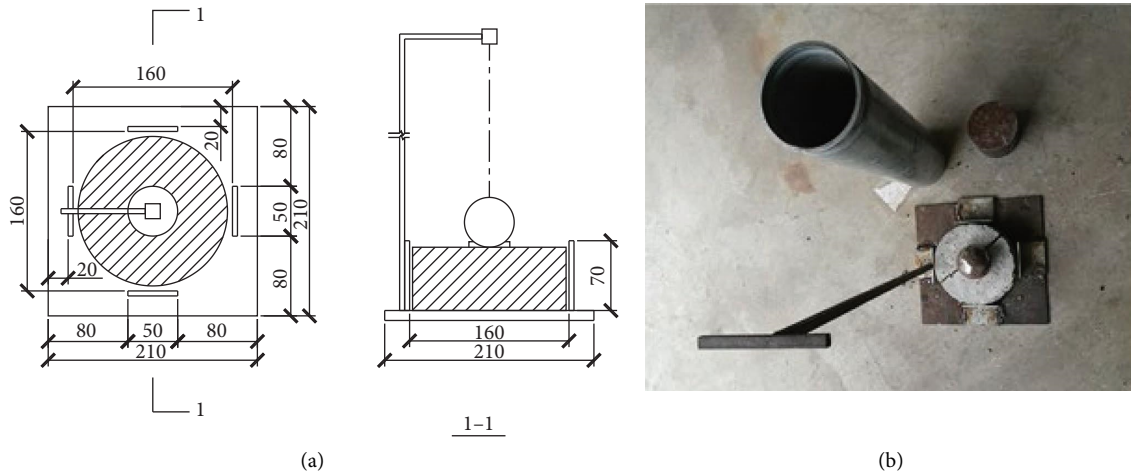
Figure 5: ARGFRC impact resistance test: (a) test setup (mm); (b) impact resistance test (top view).

$$W_1 = N_1 mgh, \tag{9}$$

$$W_2 = N_2 mgh, \tag{10}$$

where $W_1 =$ the impact energy dissipation of the initial specimen crack; $N_1 =$ the number of impact times of specimen's initial crack; $m =$ the mass of the impact hammer quality; $g =$ gravity acceleration; $h =$ the drop height of the impact hammer; $W_2 =$ the impact energy dissipation of the specimen failure; and $N_2 =$ the number of impact times of the specimen's failure.

2.3.4. SEM Test. After the flexural test, select about $1 \, cm \times 1 \, cm \times 1 \, cm$ representative samples from the fracture surface immediately for the microscopic test. When selecting the samples, try to guarantee the flatness of the observation surface of the samples. Wrap and number them in clean plastic bags to avoid contamination as much as possible. The SEM test procedure was conducted according to ASTM C1723-16 [60]. The samples were prepared with a Q150TS high-resolution magnetron ion sputtering coating machine produced by Quorum in the United Kingdom. The coating of the sample was gold, the thickness was 15.0 nm, and the density was $19.32 \, g/cm^3$. After spraying gold, the download stage was taken and fixed on the EVOMA15/LS15 tungsten filament SEM produced by Carl Zeiss, Germany. The samples were observed by adjusting the best observation distance according to the sample number.

2.3.5. EDS Test. EDS is significant accessory equipment for an electron microscope. Combined with an electron microscope, it can perform qualitative and quantitative analyses of element distribution in the microscopy area of the material. INCA X-Max 80 TEM (produced by Oxford Instrument Analysis Co., Ltd, UK) was used in the EDS test. After the concrete was stirred, the internal hydration reaction occurred, producing hydrated calcium silicate (CSH gel), calcium hydroxide, water garnet (C3AH6), ettringite, and other products. These tiny chemical products cannot be observed with the naked eye. Consequently, to better observe the GF concrete microscopically, an electron microscope was used to analyze the points of the observed sample at six thousand times magnification, and the corresponding energy spectrum observation results were presented. In the EDS analysis, the elements of the benchmark concrete sample and EDS-FC0.8 were quantitatively analyzed, and the element distribution comparison of the ARGFRC EDS-FC0 reference concrete specimen and EDS-FC0.8 were magnified 6000 times as well.

3. Results and Discussion

3.1. Cubic Compressive Strength. As the cubic compressive test results shown in Figure 6, different fiber contents had negligible impact on the early cubic compressive strength (CCS) of fiber reinforced concrete. Compared with plain concrete without fiber (CCS-FC0), when the fiber content was 0.5%, the 7 d CCS of fiber-reinforced concrete increased by 0.49%, and when the fiber content was 1.3%, the CCS decreased by 15.61%. For the 28 d CCS, the impact of different fiber contents on the strength of ARGFRC was much greater than that of the benchmark concrete (CCS-FC0). When the fiber content was 0.5%, the CCS of ARGFRC increased by 5.94%; when the fiber content was 1.5%, the CCS decreased by 11.89%; and when the fiber content was 0.3%, both the 7 d and 28 d CCS of ARGFRC were relatively increased by about 2.00%. When the fiber content was 0.5%, the CCS increased the most. The CCS of ARGFRC decreased the most when the fiber content was 1.5%. The maximum 28 d CCS for ARGFRC was 51.7 MPa (CCS-FC0.5), while the minimum 28 d CCS was 43.0 MPa (CCS-FC1.5). Consequently, it is concluded that from the influence of CCS of ARGFRC, the optimum volume fiber content was 0.5%.

3.2. Flexural Behavior

3.2.1. Load Deflection. According to the experimental data, seven different fiber contents of the ARGFRC load-deflection curve were drawn, as shown in Figure 7. For the
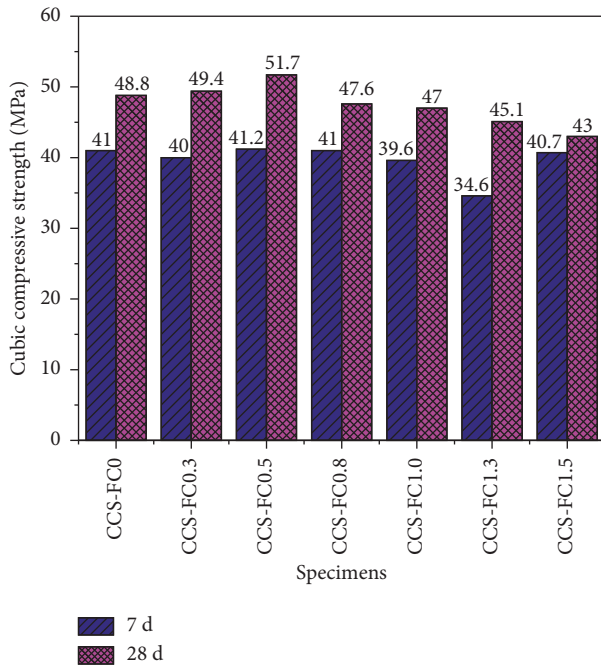
FIGURE 6: ARGFRC cubic compressive strength.

benchmark concrete FS-FC0 specimen without adding ARGF, as illustrated in Figure 7(a), the descending section was almost vertical, which fully embodied the characteristics of the brittle failure of concrete. Whereas with the emergence of ARGF addition, as specimen FS-FC0.3 illustrated in Figure 7(b), shows the decrease section of the load-deflection curve changed compared to FS-FC0, which was also a linear decrease, a similar phenomenon was shown in FS-FC0.5 (Figure 7(c)). As the ARGF fiber content gradually increased to 0.8% (FS-FC0.8), a zigzag appeared in the descent segment of the load-deflection curve, demonstrated in Figure 7(d), and the vertical decrease section became smaller than the benchmark sample (FS-FCO). Then the curve gradually deviated from the deflection axis, which illustrated that under the circumstance of the same deflection deformation, the load-bearing capacity of ARGFRC became larger, showing that ARGF was acting as a bridge relation role in concrete and increasing the ductility of concrete as provided in FS-FC0.8 (Figure 7(d)). With the constant increase of ARGF fiber content in Figures 7(e) and 7(f), dramatic changes in the load-deflection curve happened in the rising and decreasing sections. The rising section of glass fiber was slow in Figure 7(e) compared to Figure 7(d). The more apparent zigzag performance occurred in the decline section, which deviated much more from the deflection axis; the decline section in the vertical section was almost invisible but became smoother as demonstrated in Figure 7(e). ARGFs played a good role in "bridging relations," thus creating the increased concrete ductility and delaying the concrete's brittle failure. The maximum deflection of FS-FC1.3-2 in Figure 7(f) was 50% larger than FS-FC1.0-1 as shown in Figure 7(e), while the peak load of FS-FC1.3 in Figure 7(f) was smaller than FS-FC1.0 in Figure 7(e). As the specimen FS-FC1.5 load-deflection curve shows in

Figure 7(g), the decline section improved significantly, and its trend became more moderate, which turned out that with the increase of ARGF, the ductility of ARGFRC increased gradually. To facilitate the comparison of the load-deflection test results with seven different fiber contents of ARGFRC, the average value of three specimens in each group was selected to draw Figure 7(h). FS-FC0.5 indicated the largest flexural peak load (24.51 kN) among all the specimens, while FS-FC0 was the smallest flexural peak load (20.64 kN). The beam stiffness degradation phenomenon was found with the deflection increased in Figure 7(h), which was because the microcracks were initiated and the cross section was reduced with the increased loading applied to the tested beams. The average deflection of specimens (FS-FC0.8, FS-FC1.3, and FS-FC1.5) exceeded 1.4 mm, while the other four types of specimens were below 1.0 mm.

3.2.2. Flexural Strength. Table 3 depicts the calculated experimental results of the flexural test. When the fiber volume fraction addition amount was 0.5%, the strength ratio was 1.19, which could improve the maximum flexural strength of ARGFRC. As the fiber contents became 0.8% and 1.0% and the strength ratio was 1.18 and 1.17, although the flexural strength would drop slightly, compared with when the strength ratio was 1.19 and the fiber content was 0.5%, the decreasing extent was very weak. As fiber content continued to increase, flexural strength decreased gradually. When the strength ratio was 1.06, the fiber content was 1.3%, approximately the same as the reference concrete. From the flexural strength ratio, the best adding amount for a 36 mm length ARGF was 0.5%~1.0%. Figure 8(a) shows the initial crack and flexural strength curve of ARGFRC, the changing trend of experimental data could be observed from the curve. Experimental statistics indicated that mechanical performance improvements of concrete could be realized by adding a certain amount of fiber, which enhanced the toughness and cracking strength of concrete, absorbed load energy to prevent premature fracture, and improved the toughness and safety performance of the structure. Based on flexural strength test data, the last point of fiber incorporation was removed, the fiber-concrete flexural strength curve was fitted, and a unitary quadratic regression curve equation was obtained with a correlation coefficient of 0.9377, which was in good agreement with the curve.

3.2.3. Flexural Toughness Index. The arithmetic means the value calculated from the three specimens is regarded as the group specimen's flexural toughness index. The calculated values of the flexural toughness index, flexural energy, and fracture energy are demonstrated in Table 4.

Concrete without fiber content incorporation was a brittle material. The toughness index of the benchmark sample was defined as one. The toughness index of ARGFRC increased with the increase in fiber content. In Figure 8(b), the fracture energy of ARGFRC increased with the enhancement of fiber content. The value of flexural toughness I_5, I_{10}, and I_{20} was 4.0, 5.9, and 8.9, respectively, when the fiber volume content was 1.5%. Compared with benchmark
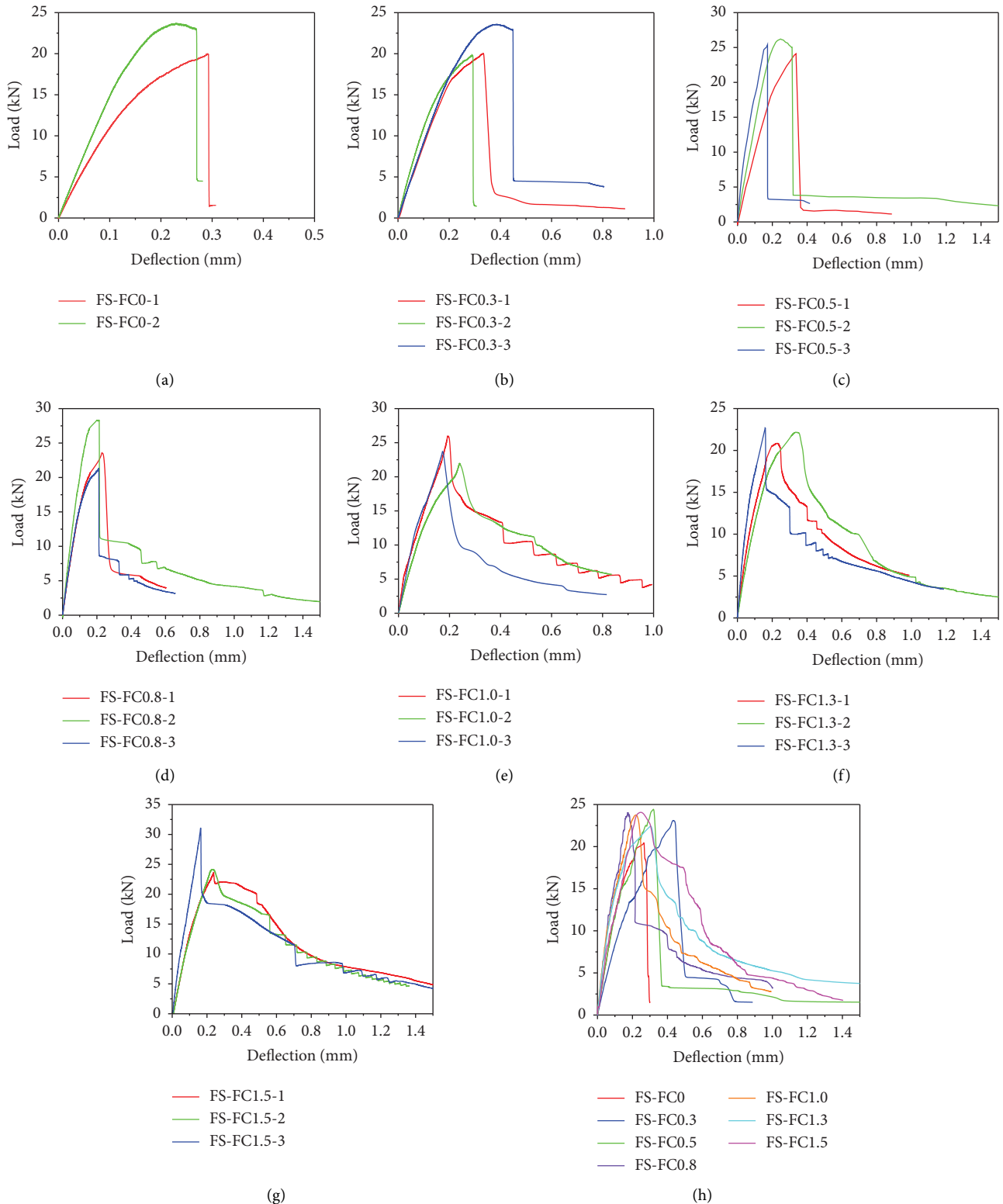
Figure 7: ARGFRC flexural load-deflection curve: (a) FS-FC0; (b) FS-FC0.3; (c) FS-FC0.5; (d) FS-FC0.8; (e) FS-FC1.0; (f) FS-FC1.3; (g) FS-FC1.5; and (h) comparison results.

samples of the concrete specimen, the flexural fracture energy of ARGFRC was improved significantly, and the flexural toughness index was increased by 3.0–7.9 times. When the fiber volume content was 1.5%, the flexural

fracture energy of ARGFRC reached its maximum value, with a maximum increase of 527.5%. In the crack propagation process, fracture energies were absorbed by the ARGFRC specimen to prevent crack development. It was

TABLE 3: ARGFRC flexural strength.

Specimens	SG	D (mm)	CP (days)	F (kN)	F_{CC} (MPa)	F_{ACC} (MPa)	f_f (MPa)	f_{cr} (MPa)	SR
FS-FC0			28	17.94 22.48 21.51	5.38 6.74 6.45	6.19	5.26	5.27	1.00
FS-FC0.3			28	24.10 22.96 20.00	7.23 6.89 6.00	6.71	5.70	5.44	1.08
FS-FC0.5			28	25.56 25.36 22.62	7.67 7.61 6.79	7.35	6.25	5.78	1.19
FS-FC0.8	C40	100 × 100 × 350	28	28.27 21.33 23.57	8.48 6.40 7.07	7.32	6.21	5.78	1.18
FS-FC1.0			28	24.18 25.96 21.99	7.25 7.79 6.60	7.21	6.13	5.61	1.17
FS-FC1.3			28	22.16 22.65 20.84	6.65 6.80 6.25	6.57	5.58	5.27	1.06
FS-FC1.5			28	31.06 23.26 24.14	9.32 6.98 7.24	7.11	6.04	5.19	1.15
	AV								1.12
	SD								0.07

Note. SG = strength grade; D = dimension; CP = curing period; F = failure load; F_{CC} = flexural strength; F_{ACC} = average flexural strength; f_f = standard flexural strength; f_{cr} = initial crack strength; SR = strength ratio; AV = average value; and SD = standard deviation.
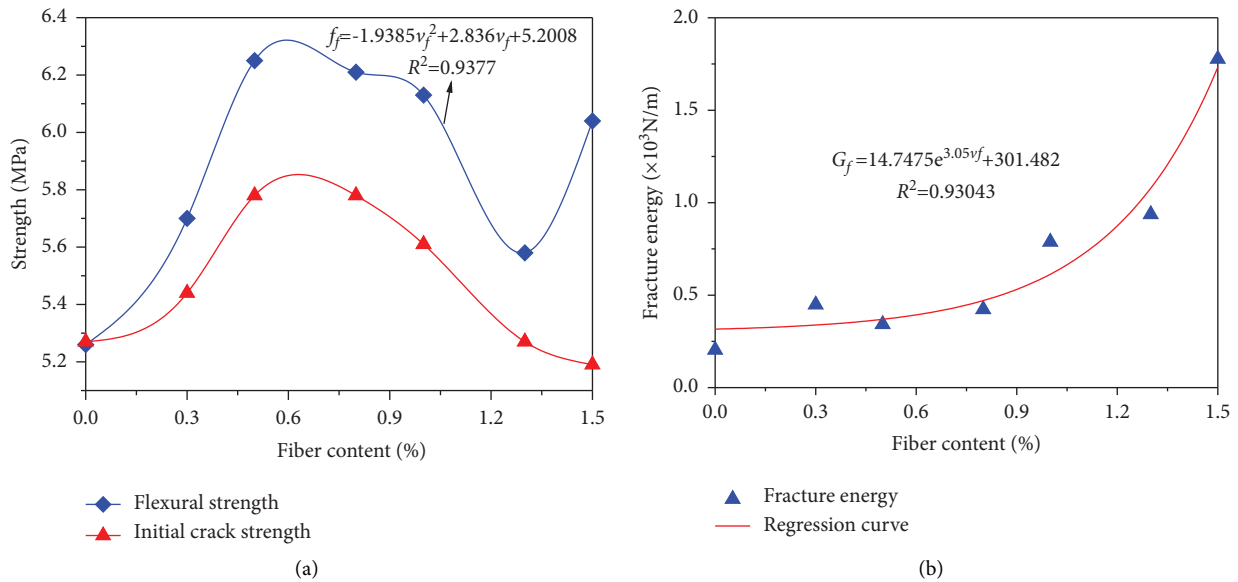

FIGURE 8: ARGFRC flexural tests: (a) flexural strength and initial crack strength; (b) fracture energy.

also available to prevent fiber breakage and concrete matrix from debonding, prevent fiber from being pulled out, and prevent damage to fiber-reinforced concrete, which was fair enough to reflect the role of fiber in concrete. Adding fibers could slow down the cracks, prevent premature cracks in the specimens, and delay the damage. As the successive increase in fiber content played a much more significant role in "bridging," the fracture energy index regression curve equation was obtained through experimental data fitting as

shown in the following Equation. The correlation coefficient was achieved with good agreement.

$$G_f = 14.7475e^{3.05v_f} + 301.482, R^2 = 0.93043. \tag{11}$$

3.2.4. Postcracking and Postpeak Toughness. Table 5 summarizes the results of the two stiffness methods. The largest value of postcracking stiffness D_{PC} was calculated as 36.174 kN/mm (FS-FC0.8), followed by the stiffness values of

TABLE 4: ARGFRC flexural toughness index.

Specimens	FVC (%)	MPL (kN)	UFS (MPa)	I_5	I_{10}	I_{20}	FEA (N·m)	FE (N·m^{-1})
FS-FC0	0.0	20.64	6.19	1.0	1.0	1.0	2.04	203.53
FS-FC0.3	0.3	22.35	6.71	1.7	2.4	3.9	4.48	448.33
FS-FC0.5	0.5	24.51	7.35	1.6	2.4	3.8	3.42	342.39
FS-FC0.8	0.8	24.39	7.32	2.7	3.9	6.1	4.23	423.31
FS-FC1.0	1.0	24.04	7.21	3.1	4.3	6.4	7.88	787.72
FS-FC1.3	1.3	21.88	6.57	3.8	5.5	8.2	9.37	936.58
FS-FC1.5	1.5	23.15	7.11	4.0	5.9	8.9	17.77	1777.15

Note. FVC = fiber volume content; MPL = the maximum peak load; UFS = ultimate flexural strength; FEA = fracture energy absorption; FE = fracture energy.

TABLE 5: Postcracking and postpeak stiffness.

Specimen	δ_{cr} (mm)	δ_{ult} (mm)	δ_{peak} (mm)	F_{peak} (kN)	F_{cr} (kN)	$F_{d,ult}$ (kN)	D_{PC} (kN/mm)	D_{PP} (kN/mm)
FS-FC0	0.14	0.30	0.27	20.64	18.45	1.46	17.631	0.002
FS-FC0.3	0.18	0.89	0.45	22.35	19.04	1.52	12.305	0.021
FS-FC0.5	0.12	0.96	0.33	24.51	20.23	2.32	20.777	0.028
FS-FC0.8	0.10	1.00	0.22	24.39	20.23	3.15	36.174	0.037
FS-FC1.0	0.07	1.20	0.24	24.04	19.64	3.48	26.377	0.046
FS-FC1.3	0.02	1.20	0.31	21.88	18.45	3.75	11.684	0.049
FS-FC1.5	0.05	1.41	0.26	23.15	18.17	5.75	23.738	0.066

FS-FC1.0, FS-FC1.5, and FS-FC0.5. The postcracking stiffness D_{PC} of FS-FC1.3 was approximately 32.3% of FS-FC0.8. Specimens FS-FC0 and FS-FC0.3 exhibited lower values (below 20 kN/mm). FS-FC1.3 presented the lowest postcracking stiffness. As for the postpeak stiffness, D_{PP}, the ascending order was FS-FC0 < FS-FC0.3 < FS-FC0.5 < FS-FC0.8 < FS-FC1.0 < FS-FC1.3 < FS-FC1.5. The test results demonstrated that the higher the fiber content, the larger the postpeak stiffness.

3.3. Impact Behavior. Each group consisted of six specimens. The maximum and minimum of the experimental data obtained were crossed out. The remaining four specimens' averaged data were represented as the experimental results of initial crack resistance energy dissipation and damage impact energy dissipation ARGFRC. ARGFRC impact resistance results are illustrated in Table 6. During the experiment process, the number and morphology of cracks were discovered to change with the variation of fiber content, as shown in Figure 9. For the benchmark specimen IR-FC0 with the fiber content of 0.0% in Figure 9(a), the initial crack was also the final crack, which was a straight-line crack through the center of the specimen, indicating that it belonged to brittle damage. Cracks were changed, obviously, after the addition of ARGF as illustrated in Figure 9(b). Three initial cracks were developed when fiber content was 0.5% in Figure 9(c), and another crack with the length of the radius was developed based on a straight line through the crack, which indicated that fiber impacted ARGFRC to restrain the generation of cracks and absorb more impact energy. As the fiber content increased to 1.0% as in the specimen IR-FC1.0 depicted in Figure 9(d), initial cracks increased to four main evenly spaced cracks that radiated from the center and took on a cross shape in Figure 9(e), which illustrated that the fiber's ability to absorb impact energy uniformly in the concrete body was better than IR-FC0.5 (Figures 9(b) and 9(c)). When fiber content was 1.5% as in specimen IR-FC1.5 in Figure 9(f), the impact number declined compared to the 1.0% dosage (IR-FC1.0), and cracks appeared obviously like a triangle with damaged cracks throughout the specimen as depicted in Figures 9(g) and 9(h). The ARGFRC impact resistance calculated results are shown in Table 6. The impact times and energy-absorbing curves from the initial crack and damaged crack were drawn, respectively, according to the test data shown in Figure 10. The curve was a fold line that suddenly began with a straight line, suddenly rose, and then fell sharply. It was gentle when fiber content was below 0.5%, but after it increased from 0.5% to 1.3%, the stroke times of the initial crack and damage state increased rapidly. When fiber content was 1.3% (IR-FC1.3), the stoke ball times of damage state compared with the benchmark concrete increased to 2363.64%, but the curve began to decline until fiber content reached 1.5% (IR-FC1.5). For the damage state, energy absorption was also raised by the increase in fiber content; the impact resistance test revealed that the increase in ARGF dramatically increased the energy absorption, and more energy would be needed to absorb in the damage process of ARGFRC compared with benchmark concrete.

3.4. SEM Analysis. The SEM observation and analysis data of ARGFRC are illustrated in Figures 11 and 12. To analyze the relationship between fiber and concrete in detail, various proportions were intercepted in the experiment. The overall density map was magnified by 1,000 times. The bonding effect of fiber and concrete was magnified by 50 times. An enlarged view of the fiber-concrete joint surface was magnified two hundred times; the overall density decreased with the increase in fiber content, but no obvious pores appeared.

TABLE 6: ARGFRC impact resistance results.

Specimens	FVC (%)	SBN (times)		EA (J)	
		N_1	N_2	W_1	W_2
IR-FC0	0.0	11	11	242.83	242.83
IR-FC0.3	0.3	10	16	220.75	353.20
IR-FC0.5	0.5	9	13	198.68	286.98
IR-FC0.8	0.8	85	99	1876.38	2185.43
IR-FC1.0	1.0	131	139	2891.83	3068.43
IR-FC1.3	1.3	260	271	5739.5	5982.325
IR-FC1.5	1.5	210	223	4635.75	4922.725

Note. IR = impact resistance; FVC = fiber volume content; SBN = sticking ball number; and EA = energy absorption.
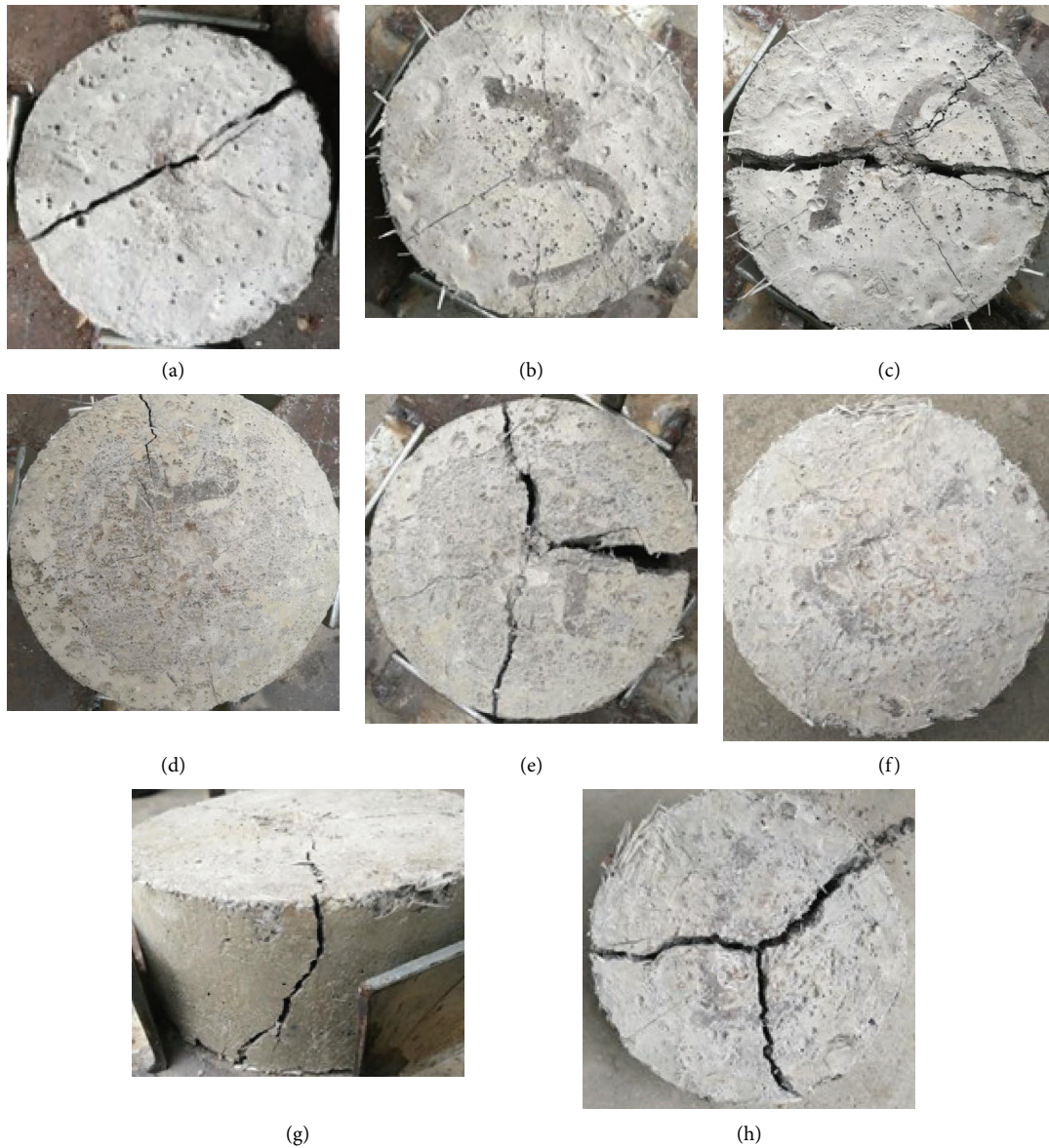

FIGURE 9: ARGFRC impact resistance crack: (a) IR-FC0; (b) IR-FC0.5 (initial crack); (c) IR-FC0.5 (damage crack); (d) IR-FC1.0 (initial crack); (e) IR-FC1.0 (damage crack); (f) IR-FC1.5 (initial crack); (g) IR-FC1.5 (side view crack); and (h) IR-FC1.5 (damage crack).

To analyze the action mechanism of ARGF in concrete more intuitively, the internal morphology of the benchmark sample FS-FC0 after flexural failure was observed by SEM.

Figure 11 suggests the microstructure (20 μm and 2 μm) of flexural test samples of concrete without ARGF (SEM-FC0). The surface of concrete without fibers contains more porous

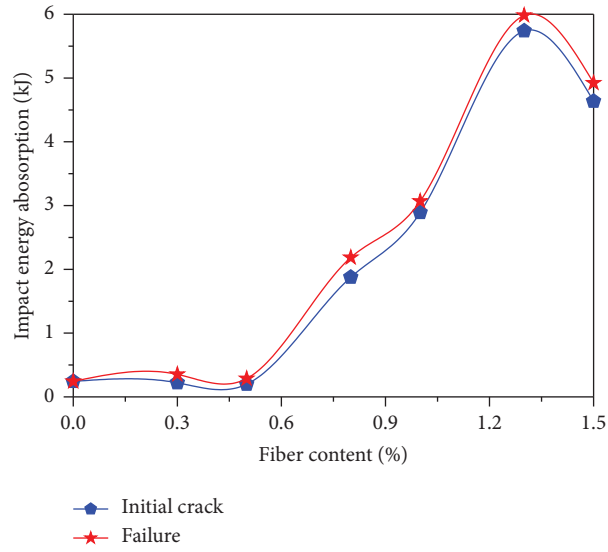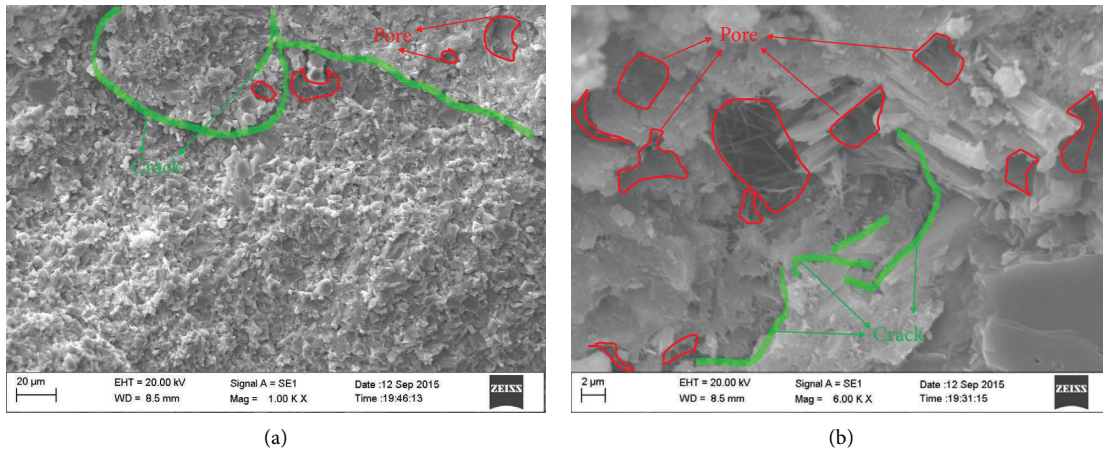Figure 10: ARGFRC impact energy absorption.

(a)

(b)

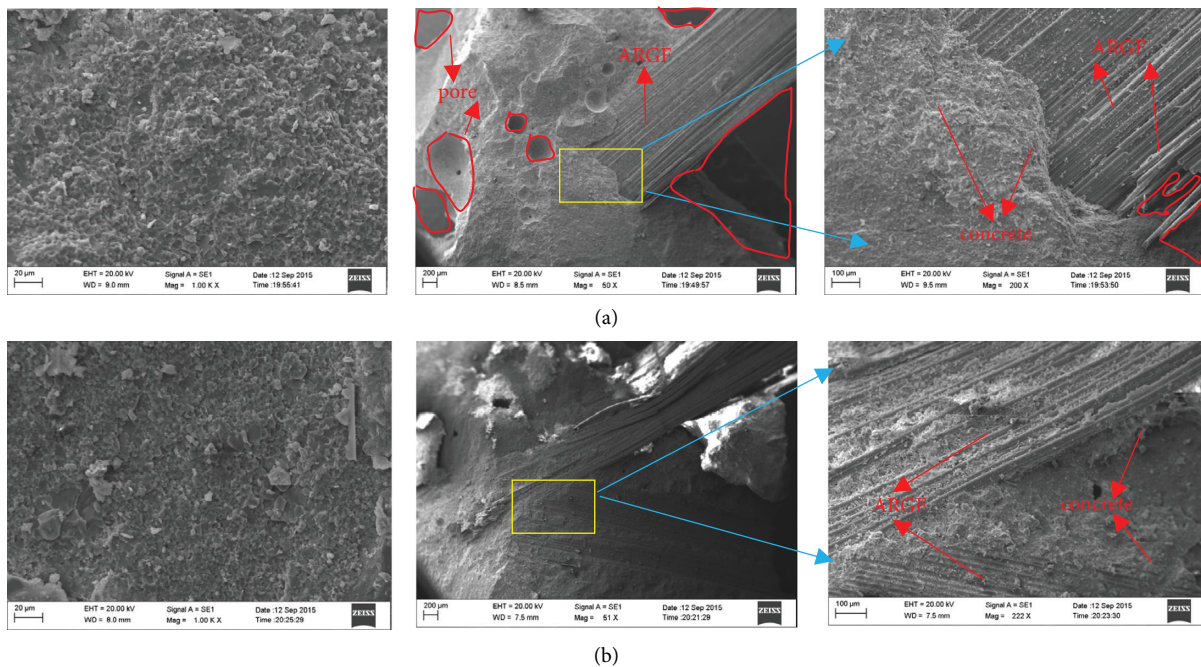Figure 11: SEM-FC0: (a) 20 μm and (b) 2 μm.
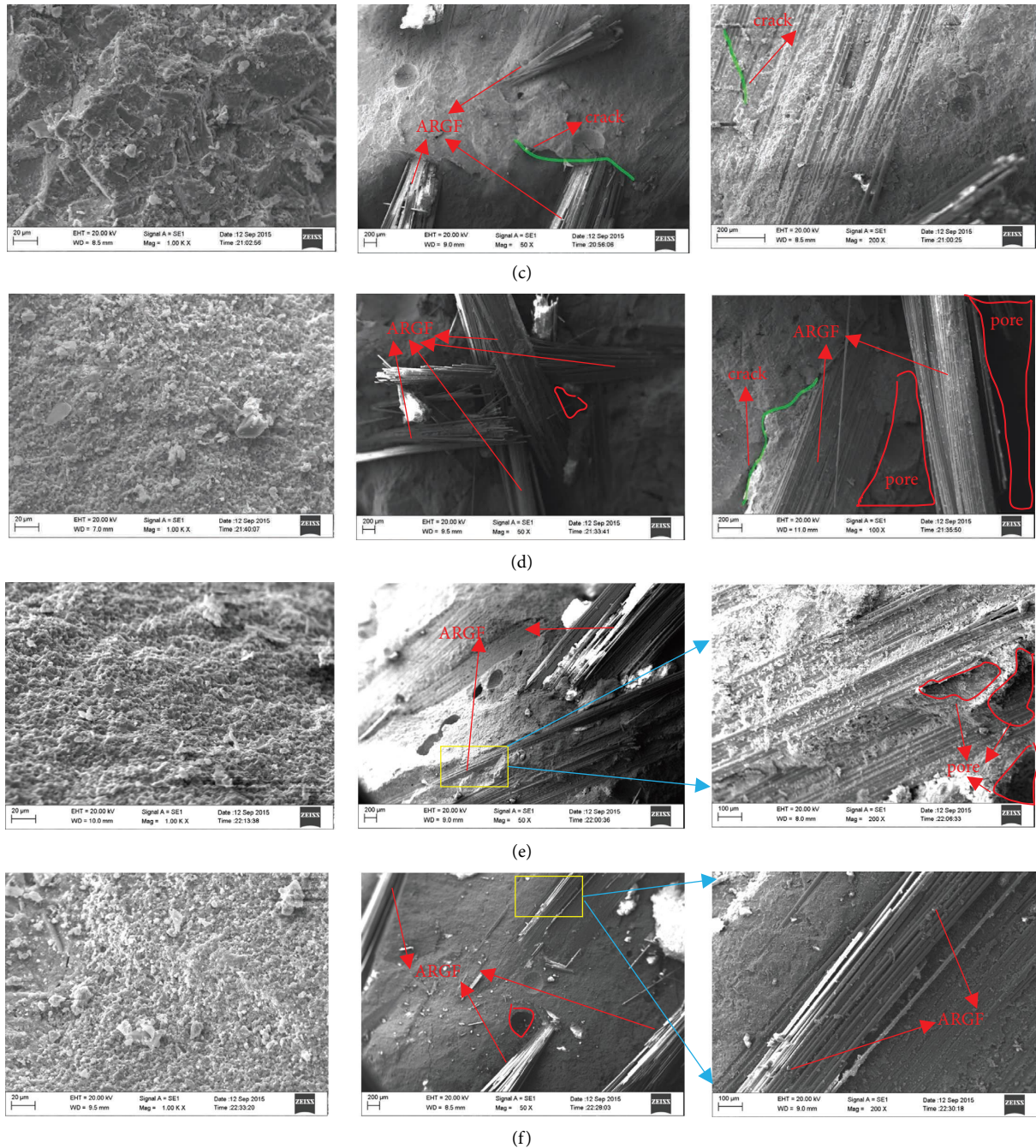

(a)

(b)

Figure 12: Continued.

Figure 12: ARGFRC SEM observation: (a) SEM-FC0.3; (b) SEM-FC0.5; (c) SEM-FC0.8; (d) SEM-FC1.0; (e) SEM-FC1.3; and (f) SEM-FC1.5.

voids and microcracks caused by hardening and shrinkage. There were two long microcracks and four porous voids as shown in Figure 11(a), while four microcracks and 11 porous voids as illustrated in Figure 11(b). The interface transition zone (ITZ) between mortar and regenerated aggregate is not close enough, and the mortar does not wrap the regenerated aggregate completely. This phenomenon accounts for the hardened hydrate formed by the hydration reaction between cement and water in the mixture attached to the aggregate surface. Meanwhile, due to the original mortar or hardened hydrate attached to the aggregate surface, the combination of cement mortar and aggregate is insufficient; the final concrete surface is insufficiently compacted; the gap at the ITZ is large; and the pore area is greatly improved. The ITZ is the weakest area, where microcracks often develop. Microcracks, voids, and ITZs are significant influencing elements of the flexural and impact behaviors of samples, which will cause excessive internal defects of concrete and ultimately decrease its mechanical properties and durability [17]. When the fiber content was 0.3%–0.8% as shown in
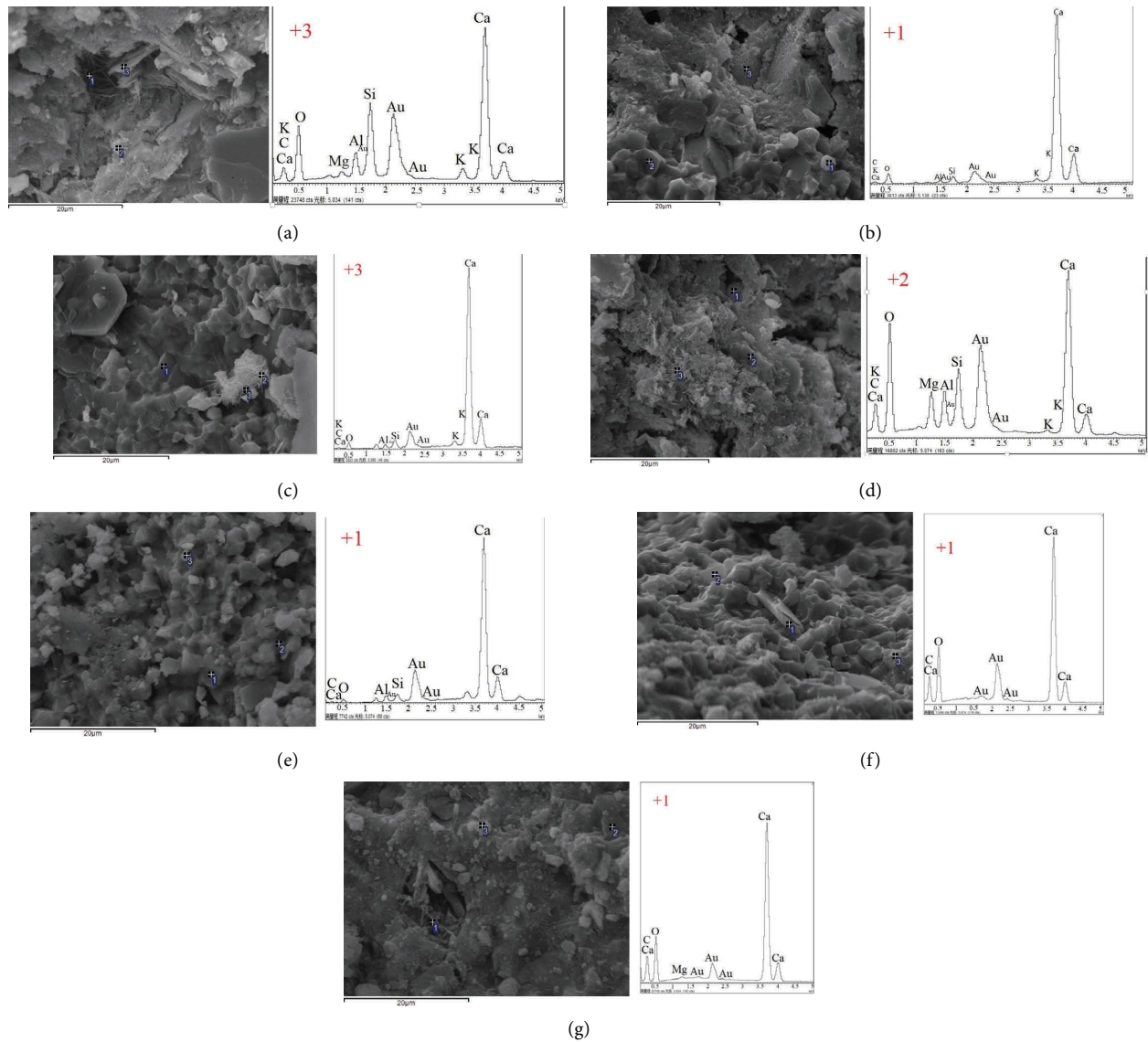
(a)

(b)

(c)

(d)

(e)

(f)

(g)

Figure 13: ARGFRC EDS observation (magnify 6000 times points analyses, energy spectrum): (a) EDS-FC0; (b) EDS-FC0.3; (c) EDS-FC0.5; (d) EDS-FC0.8; (e) EDS-FC1.0; (f) EDS-FC1.3; and (g) EDS-FC1.5.

Figures 12(a) (SEM-FC0.3), 12(b) (SEM-FC0.5), and 12(c) (SEM-FC0.8), the bond between the fibers and concrete gradually strengthened, indicating that the bond strength between the fiber and the concrete matrix was enhanced. As can be seen in Figure 12(a), there were pores in the SEM-FC0.3. The bond was not particularly good when the fiber content incorporated amount was 1.0%~1.5% as demonstrated in Figures 12(d)~12(f). There were two porous voids along the longitudinal fiber direction and a microcrack in Figure 12(d), cross fiber distribution was also found in the morphology. Figure 12(e) suggested three porous voids, which were three times as illustrated in Figure 12(f). It displayed that fiber content was not as much as possible, but there was an optimal incorporation amount of fiber content. The amount of fiber content was not better because after fiber was added, the concrete paste would affect its wrapping which will gradually decrease. When the volume of the matrix remained unchanged, the amount of mixed fiber increased. The average fiber per unit of matrix concrete wraps increased. The wrapping effect will be reduced. Microscopic tests confirmed this. When fiber content was 1.0%~1.5%, the amount of slurry that wrapped the fiber became less. It was also inconsistent with the phenomenon that during the specimen preparation process, the concrete mixer became very laborious when the fiber content reached 1.5%, as shown by SEM-FC1.5 in Figure 12(f), the concrete grout was not enough, and ARGFs were not distributed uniformly in the concrete mixture. The fracture surface occurred in Figures 12(c) and 12(d) indicated that there are many ARGFs pulled out and only a few of them were broken. Consequently, the ARGFRC flexural fracture process is greatly influenced by the fiber pull-out strength. Microcracks grow until they reach a material area that can bear the crack tip concentrate stresses that occur in front of them. More ARGFs than the nearby ones might have in this material area. The specimen bears an increased load during the

TABLE 7: EDS quantitative analyses ARGFRC EDS-FC0 and EDS-FC0.8.

Specimen	Element	Element concentration	Strength correction	Weight percentage	Weight percentage sigma
EDS-FC0	C K	45.92	0.3551	23.94	0.76
	O K	107.67	0.3339	59.72	0.62
	Mg K	1.99	0.5671	0.65	0.03
	Al K	1.89	0.6912	0.51	0.02
	Si K	9.87	0.7953	2.30	0.04
	K K	0.64	0.9966	0.12	0.02
	Ca K	63.43	0.9206	12.76	0.15
	Total			100.00	
EDS-FC0.8	C K	17.03	0.2986	21.91	1.23
	O K	46.65	0.3205	55.93	0.93
	Mg K	3.93	0.5842	2.58	0.08
	Al K	3.85	0.6862	2.15	0.06
	Si K	6.41	0.7741	3.18	0.08
	K K	0.59	0.9915	0.23	0.03
	Ca K	33.50	0.9188	14.01	0.25
	Total			100.00	

(a)   (b)
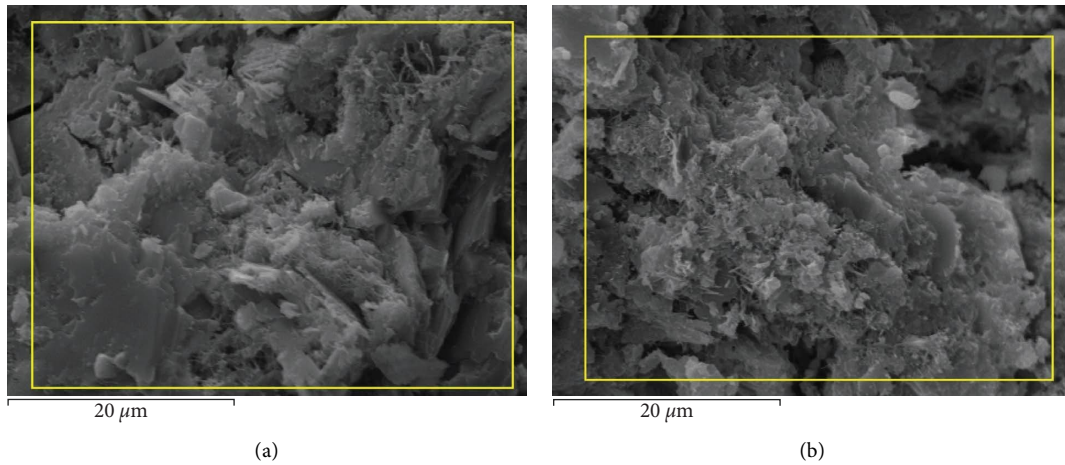
FIGURE 14: ARGFRC EDS whole surface observation (magnified 6000 times): (a) EDS-FC0 and (b) EDS-FC0.8

initiation and growth of microcracks. When it comes to the flexural strength of the ARGFRC specimen, a fracture begins to grow from the weakest microcrack, and the ARGFRC specimen will be divided into two pieces [14].

3.5. EDS Analysis. Figure 13 illustrates the magnified 6000 times point analyses and energy spectrum of the ARGFRC EDS observation results. EDS-FC0 was chosen as the benchmark specimen as shown in Figure 13(a), which was compared with EDS-FC0.8 in Figure 13(d). The EDS-FC0 result given in Figure 13(a) shows the composition of ARGFRC without fibers predominantly containing Ca, as evidenced by the large Ca peaks. The composition of specimen EDS-FC0 also contains Si, Mg, Au, and Al. In addition, porous voids at ITZ stemming from the imperfections in the cement paste were seen. The composition of ARGFRC predominantly contains Ca, as illustrated in Figures 13(b), 13(c), and 13(e). As the specimen EDS-FC0.5 shown in Figure 13(c), the test results depict that ARGFs were not distributed uniformly, and the agglomeration phenomenon was founded. The EDS result of ARGFRC with

0.8% fiber content is depicted in Figure 13(d), in which the dominant component is also Ca. In Figures 13(f) and 13(g), some gaps at ITZ stemming from the imperfect bond between ARGF and cement paste were observed. Table 7 revealed that the main hydration products of concrete were hydrated calcium silicate gel (CSH), calcium hydroxide crystals (Ca(OH)$_2$), calcium aluminate hydrate, and ettringite. The hydrated calcium sufflaminate crystals (ettringite) were easy see. The calcium element in the energy spectrum was clear, showing that even if the concrete was added with a proper amount of fiber content, the chemical reaction during the concrete mixing process was still sufficient. The production of its hydrates did not reduce. In order to better observe the distribution of elements in ARGFRC, the benchmark concrete sample (EDS-FC0) and 0.8% fiber content ARGFRC (EDS-FC0.8) were scanned on the whole surface, as shown in Figures 14(a) and 14(b). After scanning, it was clear that different chemical products were distributed 6000 times larger. It can be seen from the scanning of the cut surface of the benchmark concrete sample that the distribution of Ca elements almost occupies the whole section, and the distribution of Fe elements is

exceedingly small and almost invisible. Scanning from the surface of EDS-FC0.8 depicts that the distribution of the Ca element almost occupies the whole section, and the distribution is relatively uniform, with few Fe elements, indicating a concentrated distribution. As tabulated in Table 7, the gold distribution of the sample surface scanned from the benchmark concrete EDS-FC0, and EDS-FC0.8 was very uniform, which also determined that the gold spraying was very good in the production of specimens. The sample had good electrical conductivity during the process to ensure correct microtesting.

4. Conclusions

This research aimed to investigate the effects of fiber content (by volume) on the compressive, flexural, impact, and microstructural performance of ARGFRC. Based on the results of the experimental investigation, conclusions are drawn as follows:

(1) The flexural toughness index increased with the increase in fiber content, while the brittleness decreased. When fiber content was 1.5%, the flexural toughness I_5, I_{10}, and I_{20} values were 4.0, 5.9, and 4.0, respectively, and the corresponding flexural toughness index increased by 3.0~7.9 times.

(2) When fiber content was 1.5%, ARGFRC reached the maximum flexural fracture energy with an increment of 527.5%. The flexural toughness and the absorption fracture energy of ARGFRC improved by adding ARGF, and the flexural fracture energy increased rapidly compared with plain concrete. The flexural strength of the concrete was also affected by the variation in fiber content, and the maximum ARGFRC flexural strength was when the fiber content was at 0.5%.

(3) ARGFRC flexural strength curve was fitted with different fiber contents, and a quadratic equation of one unknown regression curve was achieved with a correlation coefficient of 0.9377. Meanwhile, fracture energy experiment data were fitted, and an exponential regression curve equation was obtained with a correlation coefficient of 0.93043.

(4) According to the flexural load-deflection curve, flexural toughness increased by adding ARGF, which could increase the ductility and delay the brittle failure when the fiber volume content reached 0.8%. The highest and lowest values of postcracking stiffness D_{PC} were calculated as 36.174 kN/mm (FS-FC0.8) and 12.305 kN/mm (FS-FC0.3), respectively. The higher the fiber content, the larger the postpeak stiffness D_{PP}.

(5) Impact resistance test results indicated that the optimum fiber volume content was 1.3%. It was recommended that fiber content be controlled within 0.5%~1.3%, and the best ratio of the fracture morphology and impact resistance absorption kinetic energy was 1.0%.

(6) The SEM analysis shows that ARGF plays a "bridging" effect in the concrete matrix, connecting cracks, and voids. The microscopic test also proved that the fiber content was not as high as possible. As the fiber content increased, the effect of the concrete grout on the fiber packaging decreased, which is why concrete flexural strength increased with the increase in fiber content.

(7) The EDS analysis indicated the distribution and content of elements in ARGFRC. The specific content of oxygen, silicon, calcium, carbon, magnesium, potassium, aluminum, and other elements was detected. Adding a certain fiber content did not affect the hydration of the concrete reaction.

Data Availability

The data used to support the findings of this study are available from the corresponding author upon request.

Conflicts of Interest

The authors declare that they have no conflicts of interest.

Acknowledgments

References

[1] W. A. Labib, *Fibre Reinforced Cement Composites*, CRC Press, London, 2018.

[2] V. Afroughsabet, L. Biolzi, and T. Ozbakkaloglu, "High-performance fiber-reinforced concrete: a review," *Journal of Materials Science*, vol. 51, no. 14, pp. 6517–6551, 2016.

[3] S. Yin, R. Tuladhar, F. Shi, M. Combe, T. Collister, and N. Sivakugan, "Use of macro plastic fibres in concrete: a review," *Construction and Building Materials*, vol. 93, pp. 180–188, 2015.

[4] D. Y. Yoo and N. Banthia, "Impact resistance of fiber-reinforced concrete – a review," *Cement and Concrete Composites*, vol. 104, Article ID 103389, 2019.

[5] J. Ahmad and Z. Zhou, "Mechanical properties of natural as well as synthetic fiber reinforced concrete: a review," *Construction and Building Materials*, vol. 333, Article ID 127353, 2022.

[6] T. A. Söylev and T. Özturan, "Durability, physical and mechanical properties of fiber-reinforced concretes at low-volume fraction," *Construction and Building Materials*, vol. 73, pp. 67–75, 2014.

[7] A. Dehghan, K. Peterson, and A. Shvarzman, "Recycled glass fiber reinforced polymer additions to Portland cement concrete," *Construction and Building Materials*, vol. 146, pp. 238–250, 2017.

[8] V. S. Gopalaratnam and R. Gettu, "On the characterization of flexural toughness in fiber reinforced concretes," *Cement and Concrete Composites*, vol. 17, no. 3, pp. 239–254, 1995.

[9] M. Bakhshi, C. Barsby, and B. Mobasher, "Comparative evaluation of early age toughness parameters in fiber reinforced concrete," *Materials and Structures*, vol. 47, no. 5, pp. 853–872, 2014.

[10] M. Madhkhan and R. Katirai, "Effect of pozzolanic materials on mechanical properties and aging of glass fiber reinforced concrete," *Construction and Building Materials*, vol. 225, pp. 146–158, 2019.

[11] V. S. Gopalaratnam, S. P. Shah, G. Batson, M. Criswell, V. Ramakishnan, and M. Wecharatana, "Fracture toughness of fiber reinforced concrete," *ACI Materials Journal*, vol. 88, no. 4, 1991.

[12] D. Vafaei, R. Hassanli, X. Ma, J. Duan, and Y. Zhuge, "Fracture toughness and impact resistance of fiber-reinforced seawater seasea-sand concrete," *Journal of Materials in Civil Engineering*, vol. 34, no. 5, Article ID 04022038, 2022.

[13] H. Kim, G. Kim, N. Gucunski, J. Nam, and J. Jeon, "Assessment of flexural toughness and impact resistance of bundle-type polyamide fiber-reinforced concrete," *Composites Part B: Engineering*, vol. 78, pp. 431–446, 2015.

[14] A. Enfedaque, D. Cendón, F. Gálvez, and V. Sánchez-Gálvez, "Analysis of glass fiber reinforced cement (GRC) fracture surfaces," *Construction and Building Materials*, vol. 24, no. 7, pp. 1302–1308, 2010.

[15] Z. Yuan and Y. Jia, "Mechanical properties and microstructure of glass fiber and polypropylene fiber reinforced concrete: an experimental study," *Construction and Building Materials*, vol. 266, Article ID 121048, 2021.

[16] A. A. Ghadban, N. I. Wehbe, and M. Underberg, "Effect of fiber type and dosage on flexural performance of fiber-reinforced concrete for highway bridges," *ACI Materials Journal*, vol. 115, no. 3, 2018.

[17] W. Yang, Z. Tang, W. Wu et al., "Effect of different fibers on impermeability of steam cured recycled concrete," *Construction and Building Materials*, vol. 328, Article ID 127063, 2022.

[18] M. Kimm, D. Pico, and T. Gries, "Investigation of surface modification and volume content of glass and carbon fibres from fibre reinforced polymer waste for reinforcing concrete," *Journal of Hazardous Materials*, vol. 390, Article ID 121797, 2020.

[19] B. Ali, L. A. Qureshi, and R. Kurda, "Environmental and economic benefits of steel, glass, and polypropylene fiber reinforced cement composite application in jointed plain concrete pavement," *Composites Communications*, vol. 22, Article ID 100437, 2020.

[20] M. Lin, S. He, S. Qiao et al., "Combined effects of expansive agents and glass fibres on the fracture performance of seawater and sea-sand concrete," *Journal of Materials Research and Technology*, vol. 20, pp. 1839–1859, 2022.

[21] M. Saidani, D. Saraireh, and M. Gerges, "Behaviour of different types of fibre reinforced concrete without admixture," *Engineering Structures*, vol. 113, pp. 328–334, 2016.

[22] Z. Çelik and A. F. Bingöl, "Fracture properties and impact resistance of self-compacting fiber reinforced concrete (SCFRC)," *Materials and Structures*, vol. 53, no. 3, p. 50, 2020.

[23] P. Aghdasi, A. E. Heid, and S.-H. Chao, "Developing ultra-high-performance fiber-reinforced concrete for large-scale structural applications," *ACI Materials Journal*, vol. 113, no. 5, 2016.

[24] J. K. Ganta, M. V. Seshagiri Rao, S. S. Mousavi, V. Srinivasa Reddy, and C. Bhojaraju, "Hybrid steel/glass fiber-reinforced self-consolidating concrete considering packing factor: mechanical and durability characteristics," *Structures*, vol. 28, pp. 956–972, 2020.

[25] S. Guzlena and G. Sakale, "Self-healing of glass fibre reinforced concrete (GRC) and polymer glass fibre reinforced concrete (PGRC) using crystalline admixtures," *Construction and Building Materials*, vol. 267, Article ID 120963, 2021.

[26] M. E. Arslan, "Effects of basalt and glass chopped fibers addition on fracture energy and mechanical properties of ordinary concrete: CMOD measurement," *Construction and Building Materials*, vol. 114, pp. 383–391, 2016.

[27] M. Khan and M. Ali, "Use of glass and nylon fibers in concrete for controlling early age micro cracking in bridge decks," *Construction and Building Materials*, vol. 125, pp. 800–808, 2016.

[28] A. B. Kizilkanat, N. Kabay, V. Akyüncü, S. Chowdhury, and A. H. Akça, "Mechanical properties and fracture behavior of basalt and glass fiber reinforced concrete: an experimental study," *Construction and Building Materials*, vol. 100, pp. 218–224, 2015.

[29] S. T. Tassew and A. S. Lubell, "Mechanical properties of glass fiber reinforced ceramic concrete," *Construction and Building Materials*, vol. 51, pp. 215–224, 2014.

[30] L. Fenu, D. Forni, and E. Cadoni, "Dynamic behaviour of cement mortars reinforced with glass and basalt fibres," *Composites Part B: Engineering*, vol. 92, pp. 142–150, 2016.

[31] F. A. Mirza and P. Soroushian, "Effects of alkali-resistant glass fiber reinforcement on crack and temperature resistance of lightweight concrete," *Cement and Concrete Composites*, vol. 24, no. 2, pp. 223–227, 2002.

[32] G. Barluenga and F. Hernández-Olivares, "Cracking control of concretes modified with short AR-glass fibers at early age. Experimental results on standard concrete and SCC," *Cement and Concrete Research*, vol. 37, no. 12, pp. 1624–1638, 2007.

[33] Y. M. Ghugal and S. B. Deshmukh, "Performance of alkali-resistant glass fiber reinforced concrete," *Journal of Reinforced Plastics and Composites*, vol. 25, no. 6, pp. 617–630, 2006.

[34] C. Scheffler, S. Zhandarov, and E. Mäder, "Alkali resistant glass fiber reinforced concrete: pull-out investigation of interphase behavior under quasi-static and high rate loading," *Cement and Concrete Composites*, vol. 84, pp. 19–27, 2017.

[35] M. Mastali, A. Dalvand, and A. R. Sattarifard, "The impact resistance and mechanical properties of reinforced self-compacting concrete with recycled glass fibre reinforced polymers," *Journal of Cleaner Production*, vol. 124, pp. 312–324, 2016.

[36] B. Ali, L. A. Qureshi, and S. U. Khan, "Flexural behavior of glass fiber-reinforced recycled aggregate concrete and its impact on the cost and carbon footprint of concrete pavement," *Construction and Building Materials*, vol. 262, Article ID 120820, 2020.

[37] B. Ali, L. A. Qureshi, S. H. A. Shah, S. U. Rehman, I. Hussain, and M. Iqbal, "A step towards durable, ductile and sustainable concrete: Simultaneous incorporation of recycled aggregates, glass fiber and fly ash," *Construction and Building Materials*, vol. 251, Article ID 118980, 2020.

[38] X. Zhao, X. J. He, and Y. C. Yang, "Numerical simulation of GFRP reinforced concrete beams," *Advances in Materials Science and Engineering*, vol. 2017, pp. 1–10, 2017.

[39] L. A. Le, G. D. Nguyen, H. H. Bui, A. H. Sheikh, and A. Kotousov, "Incorporation of micro-cracking and fibre bridging mechanisms in constitutive modelling of fibre reinforced concrete," *Journal of the Mechanics and Physics of Solids*, vol. 133, Article ID 103732, 2019.

[40] S. Yang, M. Yu, K. Dong, and Y. Yang, "Properties of alkali-resistant glass fiber reinforced coral aggregate concrete," *Materials*, vol. 13, no. 16, p. 3450, 2020.

[41] Q. Wang, H. Song, Y. Li et al., "Experimental study on the performance of graded glass fiber reinforced concrete (G-GRC) based on engineering application," *Materials*, vol. 14, no. 5, p. 1149, 2021.

[42] "GB 175-2007," *Common Portland Cement*, National Standardization Administration Committee of P.R.C, Beijing, China, 2007.

[43] "JGJ 52-2006," *Standard for Technical Requirements and Test Method of Sand and Crushed Stone (Or Gravel) for Ordinary concrete*, China Construction Industry Press, Beijing, China, 2006.

[44] GB 8076-2008, *Concrete Admixtures*, China Standard Press, Beijing, China, 2008.

[45] JGJ 63-2006, *Standard of Water for concrete*, China Construction Industry Press, Beijing, China, 2006.

[46] D.-J. Kwon, P.-S. Shin, J.-H. Kim et al., "Reinforcing effects of glass fiber/p-DCPD with fiber concentrations, types, lengths and surface treatment," *Composites Part B: Engineering*, vol. 123, pp. 74–80, 2017.

[47] ISO 1888:2006, *Textile glass-Staple Fibres or Filaments-Determination of Average Diameter*, The ISO Central Secretariat–ISO/CS, Geneva, 2006.

[48] ISO 1887:2014, The ISO Central Secretariat–ISO/CS, Geneva, Textile glass- Determination of combustible-matter content, 2014.

[49] ISO 3344:1997, The ISO Central Secretariat–ISO/CS, Geneva, Reinforcement products — Determination of moisture content, 1997.

[50] ASTM D2343-17, *Standard Test Method forTensile Properties of Glass Fiber Strands, Yarns, and Rovings Used in Reinforced Plastics*, ASTM International, West Conshohocken, PA, 2017.

[51] X. Zhao and X. J. He, "High-toughness and durability performance characterization of concrete reinforced with poly (vinyl alcohol) fibers," *Materials Express*, vol. 4, no. 3, pp. 247–252, 2014.

[52] "CECS 13-2009," *Standard Test Methods for Fiber Reinforced concrete*, China Planning Press, Beijing, 2009.

[53] GB/T 50081-2019, *Standard for Test Method of Concrete Physical and Mechanical Properties*, China Architecture and Building Press, Beijing, China, 2019.

[54] ASTM C1609/C1609M-19a, *Standard Test Method for Flexural Performance of Fiber-Reinforced Concrete (Using Beam with Third-Point Loading)*, ASTM International, West Conshohocken, PA, 2019.

[55] "ACI 544.9R-17," *Report on Measuring Mechanical Properties of Hardened Fiber-Reinforced Concrete*, American Concrete Institute, Farmington Hills, MI, 2017.

[56] JCI SF4, *Method of Tests for Flexural Strength and Flexural Toughness of Fiber Reinforced Concrete*, Japan Concrete Institute Standards for Test methods of Fiber Reinforced Concrete, Tokyo, Japan, 1984.

[57] ASTM C1018-97, *Tandard Test Method for Flexural Toughness and First-Crack Strength of Fiber-Reinforced Concrete (Using Beam with Third-Point Loading)*, ASTM International, West Conshohocken, PA, 1997.

[58] Q. Zhi and Z. Guo, "Experimental evaluation of precast concrete sandwich wall panels with steel–glass fiber--reinforced polymer shear connectors," *Advances in Structural Engineering*, vol. 20, no. 10, pp. 1476–1492, 2017.

[59] T. L. Attard and M. Soltani, "Mechanical behavior and composite action of two-wythe precast concrete sandwich beams via chemically hybridized intermediate layer," *Composite Structures*, vol. 236, Article ID 111903, 2020.

[60] ASTM C1723-16, *Standard Guide for Examination of Hardened Concrete Using Scanning Electron Microscopy*, ASTM International, West Conshohocken, PA, 2016.